analytical chemistry

Article

Cite This: Anal. Chem. 2018, 90, 8531−8537

pubs.acs.org/ac

DNA Logic Operation with Nanopore Decoding To Recognize MicroRNA Patterns in Small Cell Lung Cancer

Moe Hiratani and Ryuji Kawano*

Department of Biotechnology and Life Science, Tokyo University of Agriculture and Technology, Tokyo 184-8588, Japan

Supporting Information

ABSTRACT: Although DNA computation has traditionally been developed for parallel calculations in molecular analyses, this approach has recently been considered for use in diagnostic or medical applications in living systems. In this study, we propose that the DNA logic operation may be a powerful tool for the recognition of microRNA patterns, which may have applications for the early diagnosis of cancers. We developed a rapid, label-free decoding method for output diagnostic molecules using nanopore measurements. We designed diagnostic DNAs that autonomously recognized two microRNAs, miR-20a and miR-17-5p, and formed a four-way junction structure that was captured in the nanopore, showing long blocking currents. We analyzed the blocking duration based on the central limit theorem and found that four different operations, i.e., (0, 0), (0, 1), (1, 0), and (1, 1), could be discriminated. This pattern recognition method has been differentiated from simple detection methods based on DNA computing and nanopore technologies.

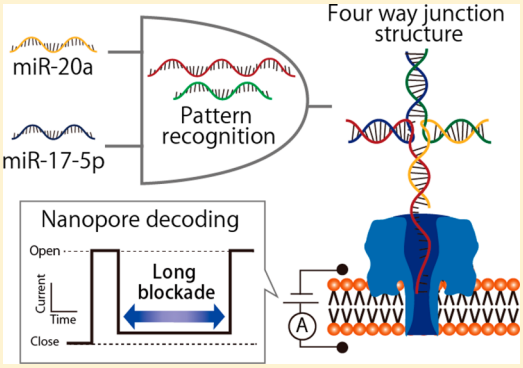

DNA computing is a useful technology for molecular calculations because it can be performed in living systems owing to its inherent biocompatibility.[1,2] Input and output molecules contain intrinsic information, such as genetic codes for proteins and recognition sites for enzymes, which can be transported under the logic operation. The decoding of information from output molecules is conventionally performed using fluorescence-based methods, which require fluorescent molecules with specific or nonspecific binding and amplification by polymerase chain reaction (PCR) and gel electrophoresis, which are time-consuming procedures.[3]

We have recently proposed methods for rapid electrical decoding using nanopore measurement,[4−7] a powerful tool for label-free, electrical detection at the single-molecule level.[8−11] In particular, α-hemolysin (αHL), which forms a 1.4 nm diameter pore in the lipid bilayer, can detect oligonucleotides precisely based on size similarities between the pore and molecules.[12−14] To apply nanopore measurements to decoding, the durability of the lipid bilayer with nanopores must be improved because the logic operation may require several hours. The conventional lipid bilayer does not have sufficient stability over long periods; it is sometimes ruptured by mechanical vibration or the applied voltage.[15,16] Several studies, including studies by our group, have described the development of stable lipid bilayer systems;[17−20] consequently, we adopted a droplet system using microfabricated devices, referred to as the droplet contact method (DCM).[21−23] A lipid bilayer is formed at the interface of the lipid monolayer with the two droplets. Based on the DCM, we have already reported parallel and stable nanopore or ion channel measurements.[24−27] Moreover, we have tested the decoding of logic operations using DNA/RNA and enzyme reactions using the droplet system; the output molecule (i.e., RNA) was detected rapidly, even when the enzyme reaction occurred in the droplet.[5]

Rapid, parallel operations using logic gates have recently been applied to the medical and diagnostic fields.[28] Benenson et al. have proposed an autonomous diagnosis and treatment approach with the logical control of gene expression.[29] Moreover, we have also proposed a "theranostics" system for cancer therapy using microRNAs (miRNAs) as input molecules; our diagnostic DNAs (dgDNAs) detected specific miRNAs from small cell lung cancer (SCLC) and formed a complex with a complementary sequence as a DNA drug (antisense drug). The antisense oligonucleotides for SCLC therapy were generated autonomously by isothermal amplification.[6] We then attempted to recognize the expression/repression patterns of miRNAs in tumor cells using DNA computing techniques.

miRNAs are potential early diagnostic markers for cancer; certain cancers secrete specific miRNAs.[30] If a single tumor secreted only a single miRNA, diagnosis would be simple; however, tumor cells show complicated miRNA expression or repression patterns.[31] For example, in a study of breast cancer, 10 miRNAs were overexpressed and 8 were downregulated, compared with expression in control tissues.[30] For conventional diagnosis using miRNAs, all miRNAs have to be analyzed quantitatively. Gu and co-workers developed a method for

Received: April 9, 2018
Accepted: April 26, 2018
Published: June 28, 2018

DOI: 10.1021/acs.analchem.8b01586
Anal. Chem. 2018, 90, 8531−8537

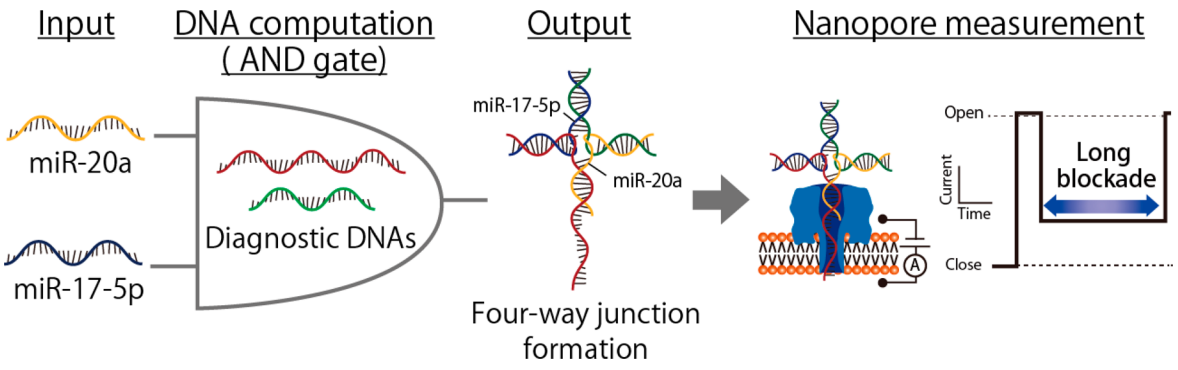

Figure 1. Schematic illustration of the AND gate for the diagnosis of small cell lung cancer. When *miR-20a* and *miR-17-5p* are overexpressed, they bind to diagnostic DNAs and form a four-way junction (4WJ) structure. Then, the 4WJ structure is captured by α-hemolysin and causes current signals with long blockades.

miRNA detection using nanopore technology with programmable polymer tags.[32−34] They also reported that nanopore measurements were superior to conventional quantitative PCR.[34]

In this study, as the first step of pattern recognition using DNA computing technology and nanopore measurement, we attempted to construct a technology for the recognition of two miRNAs secreted from SCLC using an AND operation: (0, 0), (0, 1), (1, 0), and (1, 1). Using our strategy, dgDNAs formed a 4WJ structure when *miR-20a* and *miR-17-5p* were presented, as shown in Figure 1. The 4WJ could not be translocated through the αHL nanopore and showed a long blocking current duration. In another case, dgDNA and miRNAs were single-stranded structures and passed through nanopores rapidly. To analyze the current duration in a statistical framework, we used the central limit theorem, resulting in the recognition of not only two miRNA patterns but also four different operations. Our proposed method can be used for the recognition of miRNA patterns using DNA logic operations.

EXPERIMENTAL SECTION

Reagents and Chemicals. All aqueous solutions were prepared with ultrapure water from a Milli-Q system (Millipore, Billerica, MA, USA). The reagents were as follows: 1, 2-diphytanoyl-*sn*-glycero-3-phosphocholine (DPhPC; Avanti Polar Lipids, Alabaster, AL, USA), *n*-decane (Wako Pure Chemical Industries, Ltd., Osaka, Japan), potassium chloride (KCl; Nacalai Tesque, Kyoto, Japan), and 3-(*N*-morpholino)-propanesulfonic acid (MOPS; Nacalai Tesque). Buffered electrolyte solutions (1.0 M KCl, 10 mM MOPS, pH 7.0) were prepared using ultrapure water. Wild-type αHL (Sigma-Aldrich, St. Louis, MO, USA and List Biological Laboratories, Campbell, CA, USA) was obtained as a monomeric polypeptide, isolated from *Staphylococcus aureus* in the form of a powder and dissolved at a concentration of 1 mg/mL in ultrapure water. For use, samples were diluted to the designated concentration using a buffered electrolyte solution and stored at 4 °C. High-performance liquid chromatography grade DNA oligonucleotides and miRNAs were synthesized by FASMAC Co., Ltd. (Kanagawa, Japan) and stored at −20 and −80 °C, respectively. TBE buffer (10×) was obtained from Takara Bio Inc. (Kusatsu, Japan) and was diluted 10-fold for gel electrophoresis. The power supply and an LED transilluminator were obtained from Bio Craft Co., Ltd. (Tokyo, Japan) and Optocode Corp. (Tokyo, Japan), respectively.

DNA Design and Free Energy Calculation. To confirm that DNA and miRNA hybridized as intended, a thermodynamic analysis was performed using NUPACK (California Institute of Technology, http://www.nupack.org/)[35] for each operation pattern from (0, 0) to (1, 1). This analysis was performed at 37 °C using a DNA or miRNA concentration of 3 μM in 1.0 M KCl-buffered electrolyte solution. Free energy was also obtained from the NUPACK simulation. The details of DNA design are provided below.

Design of Complementary Sequences of miR-17-5p and miR-20a in Diagnostic DNA1 and Diagnostic DNA2. The 19-mer from the 5′ terminus of diagnostic DNA1 (dgDNA1) and the 5-mer from 3′ terminus of diagnostic DNA2 (dgDNA2) formed a complementary structure with the 19-mer from the 3′ terminus and the 5-mer from the 5′ terminus of *miR-17-5p*, respectively. The 15-mer from the 3′ terminus of dgDNA1 and the 8-mer from the 5′ terminus of dgDNA2 formed a complementary structure with the 15-mer from the 5′ terminus and the 8-mer from 3′ terminus of *miR-20a*, respectively.

Thermodynamic Simulation Using NUPACK. The formation of a 4WJ structure was confirmed using the sequence designed above. The probability of 4WJ formation was 87%.

Redesign of the Sequences of dgDNA1 and dgDNA2. The complementary sequences to *miR-20a* in dgDNA1 and dgDNA2 were fixed. The complementary strand to *miR-17-5p* in dgDNA1 was shortened by one base, and the shortened sequence was added to dgDNA2.

Second Thermodynamic Simulation Using NUPACK. The formation of 4WJ was confirmed. The probability of 4WJ formation when the two bases were changed, as described above, was 92%.

Addition of the Tail Structure to the 3′ Terminus in dgDNA1. Thirty thymines were added to the 3′ terminus of dgDNA1 because this structure enabled 4WJ to enter αHL easily.

DgDNA/miRNA Hybridization. Diagnostic solutions were solutions of each miRNA pattern from (0, 0) to (1, 1) with dgDNA1 and dgDNA2 (30 μM each in 10 mM MOPS buffer; pH 7.0, containing 1 M potassium chloride). The solutions were heated to 95 °C for 5 min and then gradually cooled to room temperature.

Nondenaturing Polyacrylamide Gel Electrophoresis. 4WJ structure formation was analyzed by nondenaturing polyacrylamide gel electrophoresis (native PAGE, containing 19/1 acrylamide/bis (w/w)) on 15% gels in 1 × TBE buffer (89 mM Tris-borate, 2 mM ethylenediaminetetraacetic acid,

DOI: 10.1021/acs.analchem.8b01586
Anal. Chem. 2018, 90, 8531−8537

pH 8.3) at a constant power of 2.3 W for 40 min at room temperature. After electrophoresis, the gel was stained with diluted SYBR Green II solution (Takara Bio Inc.) for 30 min and visualized under blue LED irradiation; images were obtained using a digital camera or a FAS-BG LED BOX (NIPPON Genetics Co., Ltd., Tokyo, Japan). The fluorescence intensity of each band was calculated within square regions with the same area. Fluorescence intensity was measured five times for each band.

Ultraviolet−Visible Light Spectrum Measurement. The melting temperature for each miRNA pattern from (0, 0) to (1, 1) was analyzed by measurements of the ultraviolet−visible light (UV−vis) spectrum. The measurement solution for each pattern contained DNA and miRNAs at 1 μM each in MOPS buffer (10 mM, pH 7.0). UV−vis spectra were measured using the V-660 instrument (JASCO Corp., Tokyo, Japan) with the following settings: measurement wavelength, 260 nm; bandwidth, 2 nm; temperature, 30−80 °C for (1, 1) and (1, 0) and 30−70 °C for (0, 1) and (0, 0).

Lipid Bilayer Preparation and Reconstitution of αHL. Lipid bilayers were prepared using a device produced by microfabrication (Figure 2a). Lipid bilayers can be simultaneously formed using this device by the DCM (Figure 2b).[21,36] In this method, the two lipid monolayers contact each other and form lipid bilayers on a parylene C film, which separates the two chambers. Lipid bilayers were formed as follows. First, the wells of the device were filled with *n*-decane (2.5 μL) containing DPhPC (10 mg/mL). The recording solutions (4.7 μL) on each side of the lipid bilayers contained 1 M KCl and 10 mM MOPS (pH 7.0). αHL was reconstituted in lipid bilayers to form a nanopore from the ground side. The diagnostic solution after dgDNA/miRNA (final concentration, 3 μM) hybridization was also added to the ground side. Within a few minutes of the addition of the solutions, lipid bilayers were formed, and αHL created nanopores within them. When the lipid bilayers ruptured during this process, they were recreated by tracing with a hydrophobic stick at the interface of the droplets.

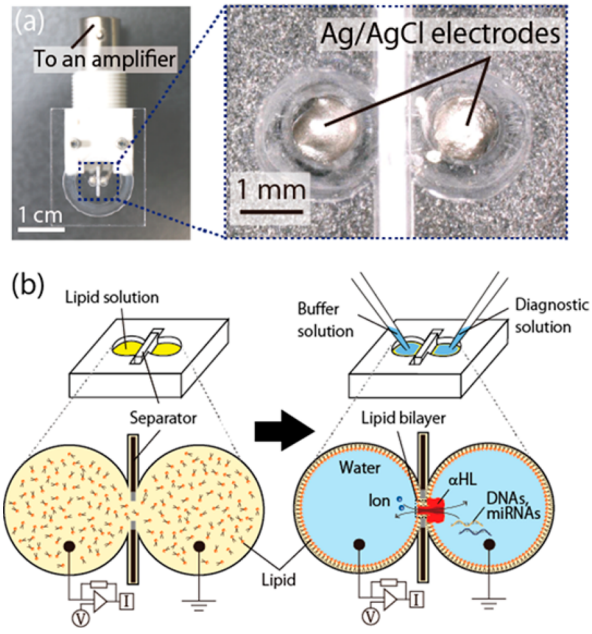

Figure 2. (a) Photograph of the devices for measuring channel currents. (b) Schematic illustration of lipid bilayer preparation.

Channel Current Measurements and Data Analysis. The channel current was recorded using an Axopatch 200B Amplifier (Molecular Devices, San Jose, CA, USA) and filtered using a low-pass Bessel filter at 10 kHz at a sampling rate of 50 kHz. A constant voltage of +150 mV was applied from the recording side, and the ground side was grounded. The recorded data from Axopatch 200B were acquired using Clampex 9.0 (Molecular Devices) with a Digidata 1440A analog-to-digital converter (Molecular Devices). Data were analyzed using Clampfit 10.6 (Molecular Devices), Excel (Microsoft, Redmond, WA, USA), and R software (R Foundation). DNA or miRNA translocation and blocking were detected when more than 85% of open αHL channel currents were inhibited. Between 347 and 500 translocating or blocking events were recorded. We examined the significance test between (1, 1) and the other systems after applying the central limit theorem: 10000 data points were extracted for each of four miRNA patterns, and the mean value was calculated by integrating 2^{16} (65536) times. Subsequently, histograms were generated from (0, 0) to (1, 1) using the data which have enough normality, and then the significance test was examined. These processes are described in a flowchart in Supporting Information Figure S1. Normality was considered statistically significant at $P < 0.05$ using Kolmogorov−Smirnov tests. Differences were considered statistically significant at $P < 0.01$ using Welch's *t*-tests. Nanopore measurements were conducted at 22 ± 2 °C.

RESULTS AND DISCUSSION

Design of Diagnostic DNAs. dgDNAs were required to form a 4WJ structure with *miR-20a* and *miR-17-5p* only when both miRNAs were present. To satisfy this requirement, we designed two dgDNAs using a thermal dynamic simulation (NUPACK) considering the following qualifications: (1) both dgDNA1 and dgDNA2 must have sequences complementary to both *miR-20a* and *miR-17-5-p* and form the 4WJ structure simultaneously with the four oligonucleotides (dgDNA1, dgDNA2, *miR-20a*, and *miR-17-5p*), and (2) 4WJ must enter an αHL nanopore after formation of the structure. Therefore, 30 nucleotides composed of polydeoxythymine (poly(dT30)) were added to the 3′ terminus of dgDNA1. The length of poly(dT30) was sufficient to reach the trans side of the αHL pore when 4WJ was captured in the nanopore. The rate of the blocking current was previously reported to be 85%.[37,38] A

Table 1. DNA and miRNA Sequences

DNA, miRNA	base sequence
dgDNA1	5′ACTACCTGCACTGTAAGACTATAAGCACTTTA$(T)_{30}$3′
dgDNA2	5′CTACCTGCCACTTTG3′
miR-20a	5′UAAAGUGCUUAUAGUGCAGGUAG3′
miR-17-5p	5′CAAAGUGCUUACAGUGCAGGUAGU3′

DOI: 10.1021/acs.analchem.8b01586
Anal. Chem. 2018, 90, 8531−8537

detailed protocol of this design is described in the Experimental Section. The most suitable sequence and the simulated structures are shown in Table 1 and Figure 3a. In addition,

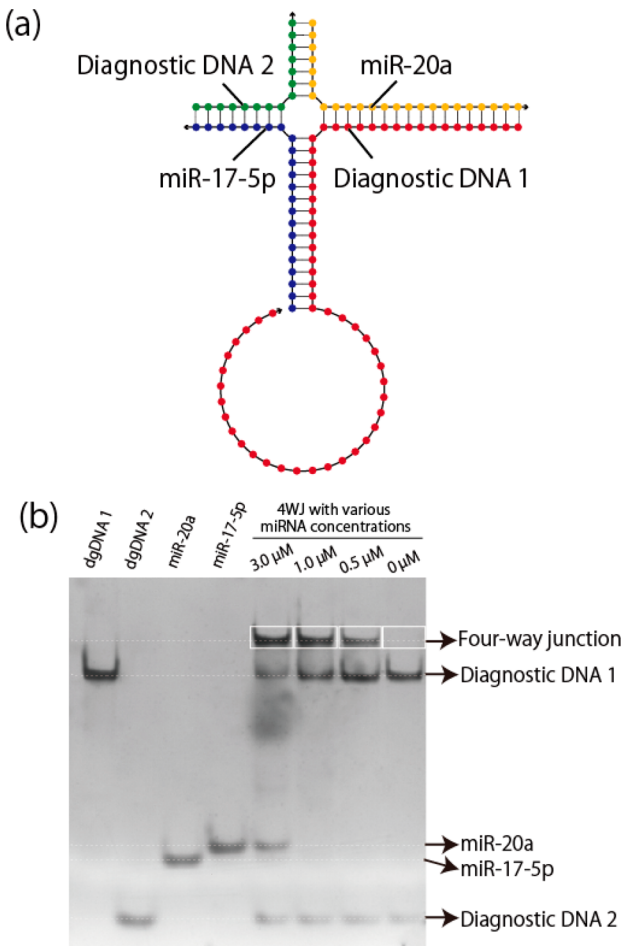

Figure 3. (a) Secondary structure of 4WJ predicted by NUPACK simulation. (b) Native PAGE image for confirmation of 4WJ formation. The 4WJ structure decreased as the miRNA concentration decreased.

all other possible binding patterns using four oligonucleotides (dgDNA1, dgDNA2, *miR-20a*, and *miR-17-5p*) were simulated (Table 2 and Figure S2). The designed 4WJ structure showed the most stable state among the possible structures.

Next, we experimentally confirmed the formation of the 4WJ structure using native PAGE. Figure 3b shows the results for each of four oligonucleotides and the two dgDNAs (3.0 μM each) with various concentrations of the target miRNAs (0−3.0 μM). For 4WJ conditions, the strength of the bands increased as the concentration of miRNAs increased, as shown in the white frame in Figure 3b. In addition, the location of the band differed from that of the (0, 1) and (1, 0) band (Figure S3). The intensities of the bands for 4WJ, dgDNA1, and dgDNA2 in Figure 3b are also shown in Figures S4 and S5. There were weak bands of unhybridized oligonucleotides, even under equal molar conditions (3.0 μM), probably due to the occurrence of nonhybridization by heat generation during gel electrophoresis. The ratio of unhybridized to hybridized molecules was estimated to be 0.5:1 (*miR-17-5p*:4WJ) based on the intensity of each band.

Table 2. Gibbs Free Energy of DNA and miRNA Combination According to NUPACK Simulations

DNA, miRNA constructs	free energy (kJ/mol)
dgDNA2	−0.00
dgDNA1	−5.10
miR-20a	−16.3
miR-17-5p	−16.3
dgDNA2 + miR-20a	−67.3
dgDNA2 + miR-17-5p	−73.6
dgDNA1 + miR-20a	−129.6
dgDNA1 + miR-17-5p	−142.2
sgDNA1 + dgDNA2 + miR-20a + miR-17-5p	−276.3

Detection of Output Molecules Using αHL Nanopores. Nanopore measurements can detect the output molecule of DNA logic operations rapidly and electrically, as we have previously shown. Therefore, in this study, we used αHL nanopores to recognize the four AND operations: (0, 0), (0, 1), (1, 0), and (1, 1). Figure 4 shows the channel current

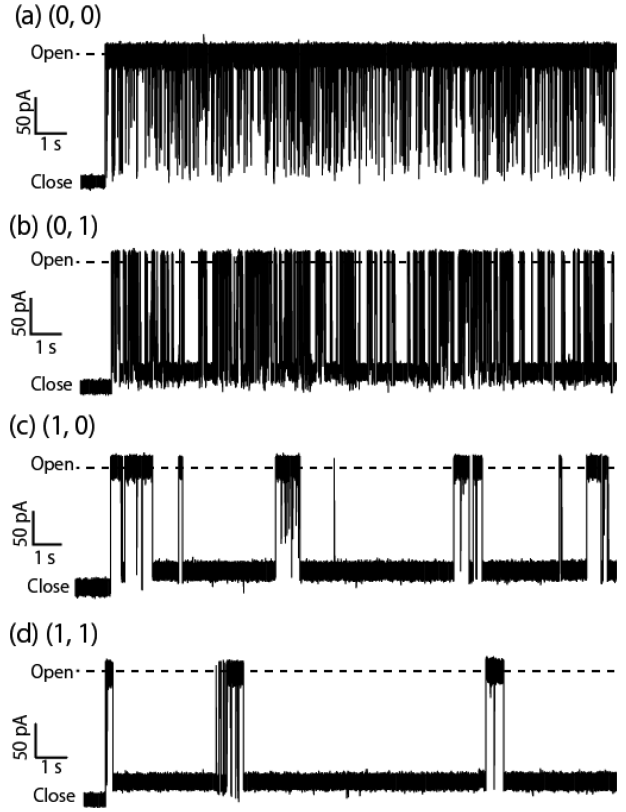

Figure 4. (a−d) Typical current and time traces of (0, 0) (a), (0, 1) (b), (1, 0) (c), and (1, 1) (d) using single αHL nanopore under 150 mV voltage application (cis side positive). The concentrations of dgDNA and miRNA were 3 μM each. The molar ratios of [dgDNA1]:[dgDNA2]:[miR-20a]:[miR-17-5p] were 1:1:0:0 in (0, 0), 1:1:1:0 in (0, 1), 1:1:0:1 in (1, 0), and 1:1:1:1 in (1, 1).

recordings for the four operations. Deep blocking currents over the 85% threshold level were observed in all four operating systems. For (0, 0), the oligonucleotides (dgDNA1 and dgDNA2) did not form hybridized structures, resulting in spike-like translocation signals of single-stranded DNA (Figure 4a). For (0, 1) and (1, 0), one of the diagnostic DNAs binds to the target miRNA and forms a weak complex. This complex initially blocks the pore and should then translocate through

DOI: 10.1021/acs.analchem.8b01586
Anal. Chem. 2018, 90, 8531−8537

the pore by unzipping the duplex (Figure 4b,c). This unzipping mechanism has been previously studied using αHL nanopores.[36,39,40] In the case of (1, 1), the four oligonucleotides formed the 4WJ structure and should block the pore, yielding long blocking duration signals (Figure 4d).

Conventionally, analyses of durations have focused on the peak of the histogram of durations or the median value because the points are not normally distributed and usually show a wide range, e.g., from approximately a millisecond to approximately a second.[40] In our case, the histogram of durations also showed an asymmetrical distribution and ranged from sub-microsecond to several tens of seconds, as shown in Figure 5 on a logarithmic scale. To discriminate between (1, 1) and the other system, we initially used *t*-tests with Gaussian fitting because the distribution seemed nearly normal. The peak durations are listed in Table 3. The peak duration increased from (0, 0) to (1, 1). We then evaluated normality using Kolmogorov−Smirnov tests to determine whether the assumptions of *t*-tests are met. Table 3 shows the results of normality tests. For all four histograms, normality was not detected ($p < 0.05$), indicating that *t*-tests could not be used to analyze durations. Therefore, we used another statistical method to evaluate durations.

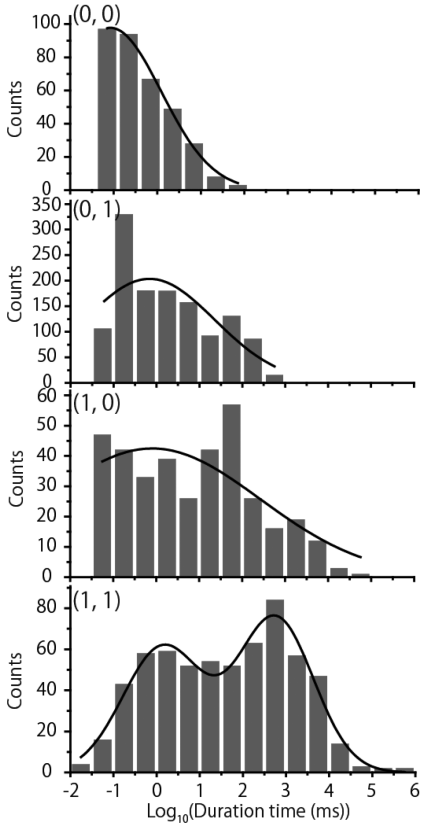

Figure 5. Histograms of the duration for each miRNA pattern. Solid lines are fits of the histograms to Gaussian curves, which were used to obtain peaks. All samples of dgDNAs and miRNAs were simple mixtures subjected to annealing treatment before obtaining measurements.

Table 3. Analysis of the Histograms Shown in Figure 5

	value of peak (ms)	normality ($p < 0.05$)
(0, 0)	0.085	no
(0, 1)	0.69	no
(1, 0)	0.81	no
(1, 1)	1.4, 575	no

Evaluation of Durations Using the Central Limit Theorem. The central limit theorem (CLT) states that the sum of a large number of random variables is approximately normal, even if the original variables themselves are not normally distributed. Based on this theorem, we generated a normal distribution from the duration data and evaluated differences using *t*-tests. The histograms of the normal distribution for the four operations are presented in Figure 6a and Figure S6.

Interestingly, each distribution gave different peak values (X_c), suggesting that all four systems had intrinsic durations. We then evaluated the intrinsic duration for each system, as follows. For (0, 0), X_c was 2.03 ± 0.0605 ms; this blocking event should reflect the translocation of dgDNA1 and dgDNA2, which formed a single-stranded state. For (0, 1) and (1, 0), the X_c values were 25.9 ± 0.707 and 728 ± 49.0 ms, respectively; the thermal dynamic simulation predicted that these formed a weakly hybridized structure comprised of the *miR-20a*/dgDNA1 (0, 1) and *miR-17-5p*/dgDNA1 (1, 0) duplexes. The hybridized free energies of the dgDNA1/*miR-17-5p* duplex were much higher than those of the dgDNA1/*miR-20a* duplex. These duplexes should translocate through the nanopore with an unzipping mechanism or eject spontaneously from the pore against the applied voltage. Finally, for (1, 1), X_c was the longest (3440 ± 292 ms), and all four oligonucleotides formed a stable 4WJ structure, resulting in the long blocking event. Additionally, X_c increased as the concentration of the target miRNAs decreased (Figure S7).

To discriminate each operation statistically, we next performed significance tests. After applying the CLT, all histograms exhibited normality. Thus, we used Welch's *t*-test to evaluate each operating system. Notably, all four systems showed significant differences ($p < 0.01$, as shown in Figure 6b). This indicated that we could use this approach to discriminate not only the two miRNAs but also all four patterns for each miRNA. Moreover, we checked the concentration dependency in this system. We set the specific duration of 4WJ to over 3148 ms based on the CLT analysis for the (1, 1) system and generated a calibration curve (Figure S8). The specific duration exhibited a linear correlation with the concentration of miRNAs.

Relationships between Duration and the Hybridized Structure. In the nanopores, the hybridized DNA blocks the pores and translocates with the unzipping of strands. The free energy of hybridized DNA is strongly related to the unzipping time in nanopore measurements. Here, we discuss this relationship for our four operation systems. The unzipping kinetics can be presented as a first-order reaction as follows:[36,40]

$$[\text{DNA/miRNA} + \alpha\text{HL}] \rightarrow [\text{single-stranded nucleic acids}] + [\alpha\text{HL}]$$

The dissociation rate constant can also be presented as follows:

$$k = k_0 \exp(-\Delta G_{sim}/N_A k_B T) \quad (1)$$

$$k = 1/t$$

where k is the dissociation rate constant, k_0 is the initial rate constant, N_A is the Avogadro constant, k_B is the Boltzmann constant used for this single molecule experiment, instead of

DOI: 10.1021/acs.analchem.8b01586
Anal. Chem. 2018, 90, 8531−8537

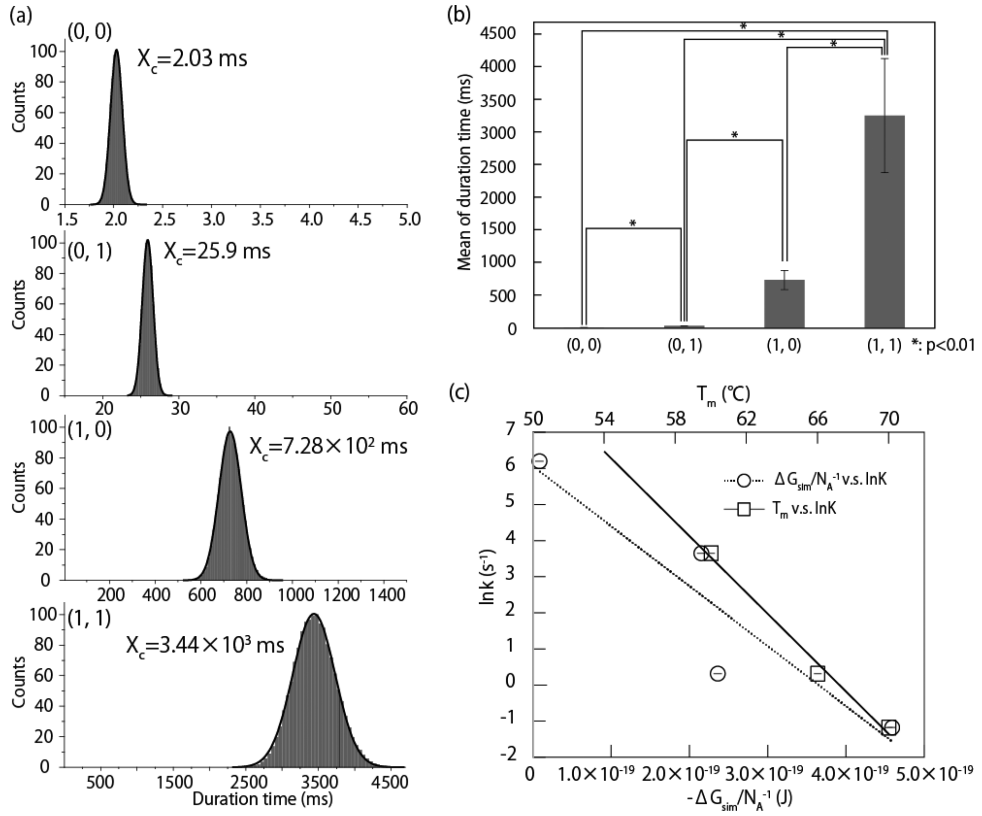

Figure 6. (a) Histograms of the duration for each miRNA pattern after data amplification based on the law of large numbers. (b) Mean value of the duration for each miRNA pattern. Error bars indicate the three-time standard deviations. (c) Correlations between the first-order rate constant and the hybridization energy (dotted line) and between the first-order rate constant and T_m (solid line).

the gas constant, T is the temperature, and t is the duration. Note that k (s^{-1}) should be equal to the inverse of t because $1/t$ is the reaction frequency per unit time in the single-molecule reaction. Figure 6c shows the relationship between the experimentally determined k and ΔG_{sim} from the thermodynamic simulation (NUPACK). The fitting result was given as $\ln k = 1.66 \times 10^{19} (-\Delta G_{sim}/N_A k_B T) + 6.06$ ($R^2 = 0.85$). Figure S9 shows the relationship between t and ΔG_{sim} for reference. Although the fitting parameters were similar to those previously reported from unzipping experiments of hairpin DNAs,[36] the correlation coefficient did not indicate sufficient linearity between $\ln k$ and ΔG_{sim}. Therefore, we next measured the melting temperatures (T_m values) of the four operating systems. This value was experimentally obtained and is plotted in Figure 6c. For (0, 0), the T_m value could not be obtained because there was no double-stranded structure. In the other systems, (0, 1), (1, 0), and (1, 1) gave melting temperatures of 61.9, 66.4, and 70.5 °C, respectively. We plotted these values and fitted them using eq 1. The fitting results yielded the equation $\ln k = -0.489 T_m + 32.8$, with a correlation coefficient of $R^2 = 0.99$. This result indicated that there was a linear correlation between T_m or ΔG_{sim} and $\ln k$. The unzipping time could be predicted by the duplex structure using the kinetic model of the unzipping events.

CONCLUSIONS

Our designed dgDNA could recognize two different miRNAs, which were found to form the 4WJ structure, resulting in long blocking signals in nanopore measurements. Statistical analysis with CLT precisely discriminated four AND operation systems: (0, 0), (0, 1), (1, 0), and (1, 1). In addition, we showed that these durations could be predicted by the hybridized strength estimated by the Gibbs free energy or the melting temperature. The selectivity of DNA hybridization with miRNA[34] and the sensitivity of nanopore detection (~1 fM)[27] would be sufficient for practical applications. Typically, in methods for miRNA detection from biofluids, such as RT-PCR or RNA arrays, the target miRNAs are extracted from real samples during pretreatment. Our method can also be combined with general pretreatment procedures before nanopore measurements. Our proposed method, based on DNA computing and nanopore technologies, is useful for miRNA pattern recognition. In future studies, we will evaluate the complex patterns of miRNAs in other cancers, e.g., bile duct cancer.

Moreover, our strategy will be integrated into the construction of a molecular robot,[41,42] i.e., a next-generation biochemical machine made of biomaterials, such as DNA, proteins, and lipids. Three prerequisites, namely, sensors, intelligence, and actuators, have been proposed for the construction of such a robot. Pattern recognition with nanopores will be a strong tool for the sensor and intelligence parts of this robot.

ASSOCIATED CONTENT

Supporting Information

The Supporting Information is available free of charge on the ACS Publications website at DOI: 10.1021/acs.analchem.8b01586.

Thermal dynamic simulation of DNAs/RNAs and fluorescent intensity of native PAGE (PDF)

DOI: 10.1021/acs.analchem.8b01586
Anal. Chem. 2018, 90, 8531−8537

AUTHOR INFORMATION

Corresponding Author

*E-mail: rjkawano@cc.tuat.ac.jp.

ORCID

Ryuji Kawano: 0000-0001-6523-0649

Author Contributions

M.H. and R.K. conceived the original idea and wrote the paper. M.H. conducted the experiments. All authors have given approval to the final version of the manuscript.

Notes

The authors declare no competing financial interest.

ACKNOWLEDGMENTS

We thank M. Takinoue (Tokyo Institute of Technology) for a useful discussion on the design of the 4WJ structure. This work was partially supported by KAKENHI (Molecular Robotics, Grant Nos. 15H00803 and 16H06043) from MEXT Japan.

REFERENCES

(1) Benenson, Y. *Nat. Rev. Genet.* **2012**, *13* (7), 455−468.
(2) Benenson, Y. *Mol. BioSyst.* **2009**, *5* (7), 675−685.
(3) Amos, M. *Theoretical and experimental DNA computation*; Natural Computing Series [Online]; Springer: New York, 2005.
(4) Yasuga, H.; Inoue, K.; Kawano, R.; Takinoue, M.; Osaki, T.; Kamiya, K.; Miki, N.; Takeuchi, S. *PLoS One* **2017**, *12* (7), e0180876.
(5) Ohara, M.; Takinoue, M.; Kawano, R. *ACS Synth. Biol.* **2017**, *6* (7), 1427−1432.
(6) Hiratani, M.; Ohara, M.; Kawano, R. *Anal. Chem.* **2017**, *89* (4), 2312−2317.
(7) Yasuga, H.; Kawano, R.; Takinoue, M.; Tsuji, Y.; Osaki, T.; Kamiya, K.; Miki, N.; Takeuchi, S. *PLoS One* **2016**, *11* (2), e0149667.
(8) Gu, L. Q.; Braha, O.; Conlan, S.; Cheley, S.; Bayley, H. *Nature* **1999**, *398* (6729), 686−90.
(9) Reiner, J. E.; Balijepalli, A.; Robertson, J. W. F.; Campbell, J.; Suehle, J.; Kasianowicz, J. J. *Chem. Rev.* **2012**, *112* (12), 6431−6451.
(10) Deamer, D. W.; Branton, D. *Acc. Chem. Res.* **2002**, *35* (10), 817−825.
(11) Howorka, S.; Siwy, Z. *Chem. Soc. Rev.* **2009**, *38* (8), 2360−2384.
(12) Kasianowicz, J. J.; Brandin, E.; Branton, D.; Deamer, D. W. *Proc. Natl. Acad. Sci. U. S. A.* **1996**, *93* (24), 13770−13773.
(13) Branton, D.; Deamer, D. W.; Marziali, A.; Bayley, H.; Benner, S. A.; Butler, T.; Di Ventra, M.; Garaj, S.; Hibbs, A.; Huang, X. H.; Jovanovich, S. B.; Krstic, P. S.; Lindsay, S.; Ling, X. S. S.; Mastrangelo, C. H.; Meller, A.; Oliver, J. S.; Pershin, Y. V.; Ramsey, J. M.; Riehn, R.; Soni, G. V.; Tabard-Cossa, V.; Wanunu, M.; Wiggin, M.; Schloss, J. A. *Nat. Biotechnol.* **2008**, *26* (10), 1146−1153.
(14) Ying, Y.-L.; Zhang, J.; Gao, R.; Long, Y.-T. *Angew. Chem., Int. Ed.* **2013**, *52* (50), 13154−13161.
(15) Mayer, M.; Kriebel, J. K.; Tosteson, M. T.; Whitesides, G. M. *Biophys. J.* **2003**, *85* (4), 2684−2695.
(16) Kawano, R.; Osaki, T.; Sasaki, H.; Takeuchi, S. *Small* **2010**, *6* (19), 2100−2104.
(17) Funakoshi, K.; Suzuki, H.; Takeuchi, S. *Anal. Chem.* **2006**, *78* (24), 8169−8174.
(18) Heron, A. J.; Thompson, J. R.; Mason, A. E.; Wallace, M. I. *J. Am. Chem. Soc.* **2007**, *129* (51), 16042−16047.
(19) Zagnoni, M. *Lab Chip* **2012**, *12* (6), 1026−1039.
(20) White, R. J.; Ervin, E. N.; Yang, T.; Chen, X.; Daniel, S.; Cremer, P. S.; White, H. S. *J. Am. Chem. Soc.* **2007**, *129* (38), 11766−11775.
(21) Kawano, R.; Tsuji, Y.; Sato, K.; Osaki, T.; Kamiya, K.; Hirano, M.; Ide, T.; Miki, N.; Takeuchi, S. *Sci. Rep.* **2013**, *3*, 1995.
(22) Kawano, R.; Tsuji, Y.; Kamiya, K.; Kodama, T.; Osaki, T.; Miki, N.; Takeuchi, S. *PLoS One* **2014**, *9* (7), e102427.
(23) Tsuji, Y.; Kawano, R.; Osaki, T.; Kamiya, K.; Miki, N.; Takeuchi, S. *Anal. Chem.* **2013**, *85* (22), 10913−10919.
(24) Watanabe, H.; Kawano, R. *Anal. Sci.* **2016**, *32* (1), 57−60.
(25) Watanabe, H.; Gubbiotti, A.; Chinappi, M.; Takai, N.; Tanaka, K.; Tsumoto, K.; Kawano, R. *Anal. Chem.* **2017**, *89* (21), 11269−11277.
(26) Kawano, R.; Horike, N.; Hijikata, Y.; Kondo, M.; Carne-Sanchez, A.; Larpent, P.; Ikemura, S.; Osaki, T.; Kamiya, K.; Kitagawa, S.; Takeuchi, S.; Furukawa, S. *Chem.* **2017**, *2* (3), 393−403.
(27) Zhang, H. L.; Hiratani, M.; Nagaoka, K.; Kawano, R. *Nanoscale* **2017**, *9* (42), 16124−16127.
(28) Jung, C.; Ellington, A. D. *Acc. Chem. Res.* **2014**, *47* (6), 1825−1835.
(29) Benenson, Y.; Paz-Elizur, T.; Adar, R.; Keinan, E.; Livneh, Z.; Shapiro, E. *Nature* **2001**, *414* (6862), 430−434.
(30) Di Leva, G.; Garofalo, M.; Croce, C. M. *Annu. Rev. Pathol.: Mech. Dis.* **2014**, *9*, 287−314.
(31) Garzon, R.; Calin, G. A.; Croce, C. M. *Annu. Rev. Med.* **2009**, *60*, 167−179.
(32) Yan, Y.; Shen, B.; Wang, H.; Sun, X.; Cheng, W.; Zhao, H.; Ju, H.; Ding, S. *Analyst* **2015**, *140* (16), 5469−74.
(33) Zhang, X. Y.; Wang, Y.; Fricke, B. L.; Gu, L. Q. *ACS Nano* **2014**, *8* (4), 3444−3450.
(34) Wang, Y.; Zheng, D. L.; Tan, Q. L.; Wang, M. X.; Gu, L. Q. *Nat. Nanotechnol.* **2011**, *6* (10), 668−674.
(35) Zadeh, J. N.; Steenberg, C. D.; Bois, J. S.; Wolfe, B. R.; Pierce, M. B.; Khan, A. R.; Dirks, R. M.; Pierce, N. A. *J. Comput. Chem.* **2011**, *32* (1), 170−173.
(36) Ohara, M.; Sekiya, Y.; Kawano, R. *Electrochemistry* **2016**, *84* (5), 338−341.
(37) Perera, R. T.; Fleming, A. M.; Peterson, A. M.; Heemstra, J. M.; Burrows, C. J.; White, H. S. *Biophys. J.* **2016**, *110* (2), 306−314.
(38) Butler, T. Z.; Gundlach, J. H.; Troll, M. *Biophys. J.* **2007**, *93* (9), 3229−40.
(39) Mathe, J.; Visram, H.; Viasnoff, V.; Rabin, Y.; Meller, A. *Biophys. J.* **2004**, *87* (5), 3205−3212.
(40) Sauer-Budge, A. F.; Nyamwanda, J. A.; Lubensky, D. K.; Branton, D. *Phys. Rev. Lett.* **2003**, *90* (23), 238101.
(41) Hagiya, M.; Konagaya, A.; Kobayashi, S.; Saito, H.; Murata, S. *Acc. Chem. Res.* **2014**, *47* (6), 1681−1690.
(42) Kawano, R. *ChemPhysChem* **2018**, *19* (4), 359−366.

DOI: 10.1021/acs.analchem.8b01586
Anal. Chem. 2018, 90, 8531−8537